CrossMark

ORIGINAL RESEARCH

Synthesis and Performance of Nickel/Reduced Graphene Oxide Hybrid for Hydrogen Evolution Reaction.

Esteban A. Franceschini[1,2] · Gabriela I. Lacconi[1]

Abstract In this work, a simple and reproducible method for the syntheses of hybrid nickel/reduced graphene oxide electrodes is presented. This method consists in a direct modification of a conventional nickel electrodeposition bath, making the synthesis industrially scalable. The synthesized catalyst is structural and electrochemically characterized and compared to the traditional electrodeposited nickel. The kinetics of hydrogen evolution reaction (HER) is studied on both conventional nickel watts (Ni-watts) and nickel/reduced graphene oxide hybrid (NirGO). An increment in the catalytic activity is observed along with the absence of nickel hydrides. Thus, the NirGO catalyst presents a higher catalytic activity towards HER, and the presence of graphene in the Ni matrix inhibits the nickel hidruration.

Keywords Nickel · Reduced graphene oxide · Catalyst · Hydrogen evolution reaction · Co-deposition

✉ Esteban A. Franceschini
estebanfranceschini@yahoo.com.ar

1 INFIQC-CONICET, Dto. de Fisicoquímica–Facultad de Ciencias Químicas, Universidad Nacional de Córdoba, Ciudad Universitaria, 5000 Córdoba, Argentina

2 Departamento de Física de la Materia Condensada, Centro Atómico Constituyentes, Comisión Nacional de Energía Atómica, B1650KNA Buenos Aires, San Martín, Argentina

Introduction

Hydrogen has attracted recent attention as a clean energy vector, which can be used in fuel cells, or in replace of natural gas in the so-called "hydrogen economy" [1–4]. Hydrogen production through water electrolysis is considered to be the cleanest production way for hydrogen economy in the near future [5, 6].

To improve the electrocatalytic activity of the catalysts for the electrochemical reactions, two approaches are usually employed in the literature: first, the change of the extrinsic property of electrocatalysts, for instance, modifying the surface area, the surface morphology [7, 8] or the particle size [9] of the electrocatalysts. The second way is by the change of the intrinsic property of the electrocatalysts, for example, changing the alloy composition [10, 11] or coupling different multifunctional materials [12, 13] to change the electron configuration of the electrocatalysts. Thus, the use of nanomaterials as new building blocks to create light energy assemblies has opened up new ways to utilize renewable energy resources [11, 14]. It has recently been reported that carbon-based nanomaterials as graphene oxide (GO) exhibit superior performance in electrodes for lithium-ion batteries [15, 16], supercapacitors [17–19], and electrodes for HER [20–22].

Reduced graphene oxide exhibits many unique properties, such as large theoretical specific surface area ($2630 \text{ m}^2 \text{ g}^{-1}$), fast room temperature mobility of charge carriers ($2 \times 10^5 \text{ cm}^2 \text{ V}^{-1} \text{ s}^{-1}$), excellent optical transmittance ($\sim 97.7\%$), and exceptional conductivity (10^6 Scm^{-1}) [23]. These outstanding properties are indicatives that reduced graphene oxide has great potential to be an ideal construction component of hybrid electrode materials for hydrogen production.

Seetharaman et al. [24] reported the performance of GO modified with non-noble metal-based electrode in alkaline

🖄 Springer

anion exchange membrane electrolyzer. They used an electrode with a ternary alloy of Ni as cathode and oxidized Ni electrode coated with graphene oxide as anode. The electrochemical activity of the GO-modified electrode was higher than the uncoated electrode. The current density for HER at 30 °C was 50% higher for the anion exchange membrane water electrolyzer with the modified electrode compared to that obtained on an uncoated electrode at 2 V.

Yang and coworkers [13] have presented a NiAl-layered nanosheet array, grown on a graphene oxide substrate by a hydrothermal method, which is used as precursor to a N-doped carbon electrode by coating with dopamine followed by calcination. The electrode is used as a non-noble metal electrocatalyst for hydrogen evolution reaction in alkaline medium, exhibiting high electrocatalytic activity with low onset overpotential (− 75 mV). Although it presents some improved electrocatalytic characteristics, its synthesis method requires a complex series of steps, including high temperatures (700 °C) and long drying times. On the other side, Wang and coworkers have presented a method for the electrodeposition of graphene sheets on nickel foams as supercapacitor electrodes [25]. The electrodeposition process was accomplished by electrochemical reduction of GO in its aqueous suspension. The electrolyte was a solution of $LiClO_4$ containing a graphene oxide suspension. The porous graphene/nickel foam electrodes exhibited excellent double-layer capacitive properties with high rate capability, remarkable cycle stability, and high specific capacitance of 183.2 mF cm^{-2} at the current density of 1 mA cm^{-2}.

In this work, a simple and reproducible method for the synthesis of a nickel/reduced graphene oxide hybrid electrode (NirGO) for the hydrogen evolution reaction is developed. The method consists in the direct modification of a conventional nickel watts electrodeposition bath, without requiring high temperatures, long reaction times, or complex synthesis steps. The hybrid material synthesized was characterized as electrode for the hydrogen evolution reaction in alkaline medium. All the catalysts synthesized were characterized before and after a short aging process in order to characterize the changes in the catalytic activity due to surface modification originated by hidruration of the surface.

Experimental

Chemicals and Materials

Nickel sulfate (Anedra, PA grade), nickel chloride (Merck, PA grade), boric acid (Merck, PA grade), ethanol 96% (Cicarelli, PA grade), hydrochloric acid 36.5–37% (Cicarelli, PA grade), potassium hydroxide (Anedra RA reagent), and graphene oxide dispersion (Graphenea Inc.) were used as received. All

solutions were prepared with Milli-Q water and degassed employing high purity N_2 (Indura S.A.).

Catalyst Synthesis

The catalysts were synthesized using a conventional Ni watts electrodeposition bath prepared by dissolution of 25 g of boric acid in water at 50 °C. Nickel sulfate of 240 g and then 25 g of nickel chloride were added to the boric acid solution under constant stirring to obtain 1 L of solution. This watts electrodeposition bath was used to synthesize a conventional electrodeposited nickel catalyst.

Part of that Ni watts bath was separated to prepare a modified Ni/graphene oxide bath to obtain the NirGO hybrid catalyst. For that, a 0.08-g L^{-1} GO dispersion was sonicated during 30 min in order to disperse the GO flakes, and then 10 mL of the GO dispersion was added to 40 mL of the watts bath.

The synthesis of both catalysts was carried out by electrodeposition on a commercial Ni electrode (RC S.A. 99.9 purity), with a circular area of 0.196 cm^2, which is mounted on a rotating disk electrode (RDE) support (Pine Research Inst.; Raleigh, NC). The nickel electrodes were polished with 0.05 μm alumina, cleaned with ethanol, and pretreated with consecutive immersion steps in KOH (1 M) and HCl (10% w/w) solutions in order to clean the surface. Synthesis of both catalysts were carried out in a two electrode electrochemical cell thermostatized at 50 °C, using a massive nickel counter electrode with high surface area. During the process, the homogeneity of the electrodeposits was controlled maintaining the working electrode at a rotation rate of 1600 rpm. Moreover, the working electrode rotation facilitates that the species in the solution (Ni ions and GO flakes) reach the surface of the electrode.

The current applied during the synthesis of both Ni-watts and NirGO catalysts was 0.05 Acm^{-2} for 3600 s, in order to obtain a deposit thickness of around 60 μm. During the electrodeposition of both catalysts, the potential-time transient attained around 5 V, which indicates that the co-deposited GO flakes should be in a reduced state, it is under these conditions where the graphene is highly conductive [26].

After the synthesis, both catalysts were washed repeatedly with milli Q water in order to remove the rest of the electrodeposition bath over the electrode surface.

Structural Characterization

Scanning electron microscopy images were obtained with a Supra 40 FESEM (Zeiss Company) operating at 8 kV. EDX spectra and mapping were obtained operating at 10 kV. The samples scratched from the RDE electrodes were electrodeposited, in order to obtain the SEM images properly.

Raman spectra of the electrode surface were acquired with a LABRAM-HR, Horiba Jobin-Yvon Raman microscope with

a 100× objective lens (NA = 0.9). The laser excitation was 488.0 nm (Ar laser). The illuminated area in all Raman experiments was 1.0 μm^2 with a spectral resolution of 1.5 cm^{-1}. At least five different zones on each sample were analyzed, to confirm the homogeneity of the catalysts.

X-ray diffractograms were measured using the λ = 1.5406 Å Cu Kα radiation, employing a PANalytical X'Pert PRO diffractometer operating at 40 kV and 40 mA, in the θ–2θ Bragg–Brentano geometry. All measures were carried out at room temperature. The 2θ range used was between 10° and 70°, with 0.02° steps and counting time of 2 s per step. The Rietveld method was used to refine the crystal structure employing the FULLPROF program [27]. A pseudo-Voigt shape function was used to fit the experimental data. The data refined were lattice parameters, atomic positions, isotropic thermal parameters, peak shape, and occupation factors. The sample of Ni electrodeposited from watts bath (Ni-watts) was measured directly from the massive electrode, while the analysis of NirGO sample requires detachment of the material from the RDE electrode. It explains the intensity differences observed in the diffractrograms.

Electrochemical Characterization

All the electrochemical characterization experiments were carried out in a conventional three-electrode electrochemical cell with a thermostatic jacket. One molar KOH aqueous solution was used as electrolyte, and during the electrochemical measurements, a high purity nitrogen flux was maintained over the electrolyte surface for proper deaeration of the solution. A saturated calomel electrode (SCE) was used as reference electrode (0.243 V vs. RHE) and a large area platinum foil as counter electrode. The reference electrode was kept at room temperature, and the circuit was closed using a capillary luggin. All the reported potentials were referred to the reversible hydrogen electrode (RHE).

The electrochemical studies were conducted with an Autolab PGStat30 potentiostat/galvanostat coupled to a FRA2 module. RDE measurements were performed with a Ni disk electrode mounted in an interchangeable RDE holder (Pine Research Inst.; Raleigh, NC) where the catalysts are electrodeposited, and the rotation rate was varied between 100 and 2500 rpm. The uncompensated ohmic drop correction was carried out as presented elsewhere [30]. The temperature of the electrochemical cell was controlled using a Lauda Alpha RA 8 controller. The area used for all current density calculation was 0.196 cm^2 (the geometric area of the disk electrode). Cyclic voltammetry (CV) and linear sweep voltammetry (LSV) experiments were conducted between 0.344 and − 1.256 V (vs. RHE) at a scan rate of 10 mV s^{-1} for all electrodes.

Electrochemical impedance spectroscopy (EIS) experiments were carried out at frequencies between 10 mHz and 100 kHz applying a 10-mV potential modulation at different electrode potentials, such as open circuit potential (OCP), HER onset potential (OP), 0.1 and 0.3 V more cathodic than the corresponding OP of each catalyst. These potential values were selected in order to cover the potential range where the HER occurs [27]. The ZView 3.3 program (Scribner Associates, Inc.) was used to fitting the measured data in the interval frequencies between 10 mHz and 100 kHz with a modification of the equivalent circuit proposed by Armstrong and Henderson [28, 29]. Chronoamperometric profiles were obtained by applying a potential pulse of − 1.256 V (vs. RHE) during 4 h at 298 K in order to study the changes that occurred in the electrode surfaces after a short aging process. A 900-rpm electrode rotation rate was used for the EIS and chronoamperometric experiments, in order to prevent the formation of bubbles.

Electrocatalytic Activity

The electrocatalytic activity of an electrode in relation of a particular reaction can be related to different electrochemical parameters. The current density is strongly influenced by parameters such as the exchange current (j_0), the onset potential (OP), and the dj/dV slope. The OP is presented as an important factor since for the same dj/dV slope, the catalyst with a lower OP presents a higher current density and therefore, greater catalytic activity.

The electrochemical analysis was carried out as was presented elsewhere [30, 31]. The HER overall current density (j) can be expressed in terms of the Koutecky–Levich (K–L) equation:

$$\frac{1}{j} - \frac{1}{j_k} + \frac{1}{j_d} = \frac{1}{j_k} + \frac{1}{B\omega^{1/2}} \tag{1}$$

where j_k is the mass transfer corrected kinetic current density, j_d the boundary-layer diffusion limited current density, ω is the rotation rate (rpm), and B is the Levich slope. The theoretical Levich slope (B) for single electron charge transfer (i.e., $n = 1$) process is 59.20 mA cm^{-2} rpm$^{-1/2}$. Comparison between experimental and theoretical B values allows evaluating the number of electrons involved in the reaction. In this way, the corrected current density (or kinetic current density) is used to construct Tafel plots in order to calculate the exchange current (j_0) and the Tafel slope parameter (b).

The Tafel equation is as follows:

$$\log j_k = \frac{2.3RT}{nFa}E + j_0 = bE + j_0 \tag{2}$$

where b is the Tafel slope parameter, n is the number of electrons transferred, α is the transfer coefficient, and j_0 is the exchange current. In order to calculate the n value, we suppose a $\alpha = 0.5$. The j_k was calculated by correcting the

measured j by the mass transfer using the j_d, with Eq. (3):

$$j_k = j\left(\frac{j_d}{j_d - j}\right) \tag{3}$$

Results and Discussion

Catalyst Structural Characterization

The catalysts obtained with different electrodeposition baths have very different optical properties. While the Ni-watts electrode is dull gray, NirGO electrode is black, suggesting that the presence of GO reduced in the matrix of the catalyst and homogeneously distributed on the surface.

Scanning electron micrographs were obtained in order to analyze the morphology and the presence of crevices in both electrodeposited catalysts. SEM micrographs of Ni-watts catalyst (Fig. 1a) show a homogeneous granular structure. In Fig. 1b, c, the SEM micrographs of the NirGO electrode at different magnifications are presented. The samples are mainly granular; neither polishing marks nor superficial fractures are evidenced. It can be seen, particularly at low magnifications (Fig. 1b), that the reduced graphene oxide flakes are distributed over the NirGO electrode surface. The backscattering image (not shown) indicates that those flakes have a lower electronic density than the rest of the sample, confirming the presence of graphene flakes.

Analysis of chemical composition by EDS shows no metallic contamination of the samples, and only traces of Al and Si (from the mechanical polishing) are observed. EDS mapping shows a homogeneous composition of Ni and C on the whole sample surface. However, this analysis is not enough for quantification since carbon contamination from the environment is always present, for example from the conductive tape used.

Raman spectra recorded from both catalysts are shown in Fig. 2, along with the commercial GO spectrum (supported on a silicon wafer) with comparative ends. The obtained spectra in different areas of each sample do not show significant differences. The scattering spectra from the Ni-watts electrode do not show peaks, indicating that the nickel is in a metallic state and there is no signal of nickel hydrides, since those materials show Raman bands at 3581 and 3660 cm^{-1} [32]. The NirGO electrode spectrum shows the GO characteristic bands, evidencing the presence of graphene intercalated in the structure of the nickel electrodeposits.

Raman spectroscopy is widely used to characterize the structure, chemical nature, and defects in graphene-based materials [33]. The reduction process of GO to give reduced graphene oxide (denoted as rGO) can manifest itself in Raman spectra by the changes in the relative intensity of two main
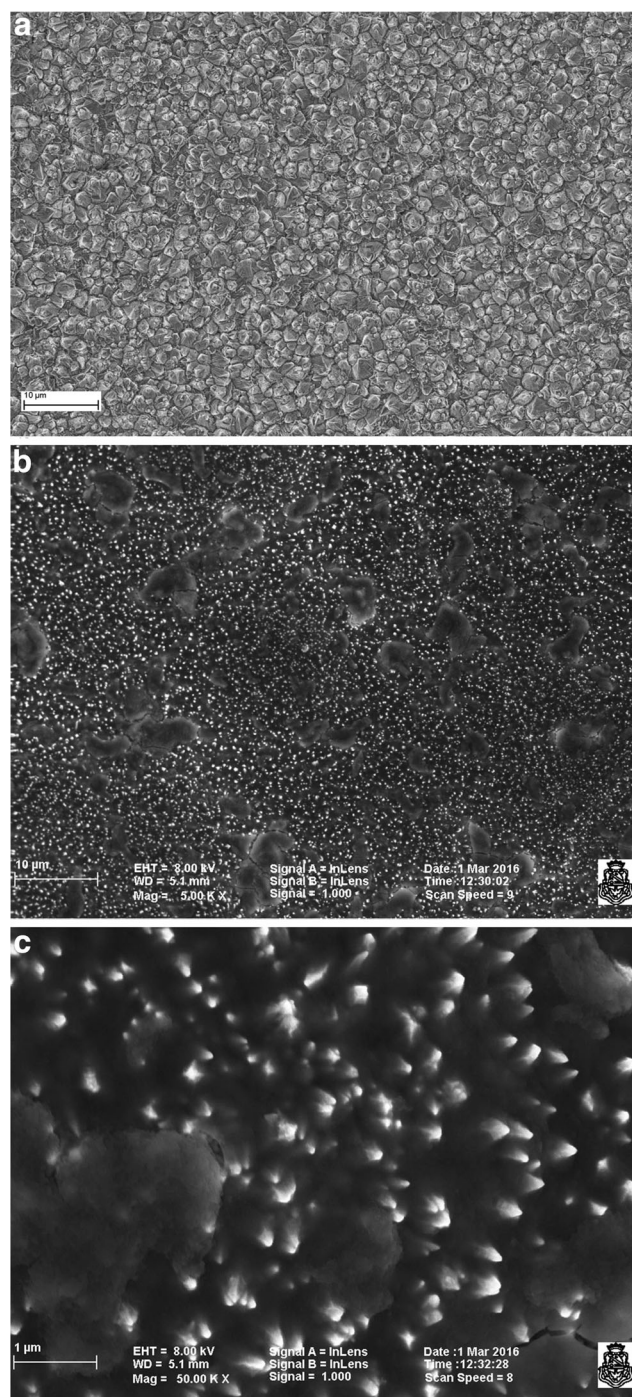

Fig. 1 SEM micrograph of **a** Ni-watts (magnification of 5000×). **b** NirGO (magnification of 5000×). **c** NirGO electrodeposition (magnification of 50,000×). All samples were measured at 8 keV

peaks: D and G [34]. Figure 2 shows the Raman spectra of commercial GO and NirGO electrodeposited on nickel electrode where the D and G peaks are observed. The D peak of GO located at 1349 cm^{-1} comes from a defect-induced breathing mode of sp2 rings and arises from the stretching of C–C bond with an intensity related to the size of the in-plane sp2 domains [26]. The G peak at 1601 cm^{-1} for GO
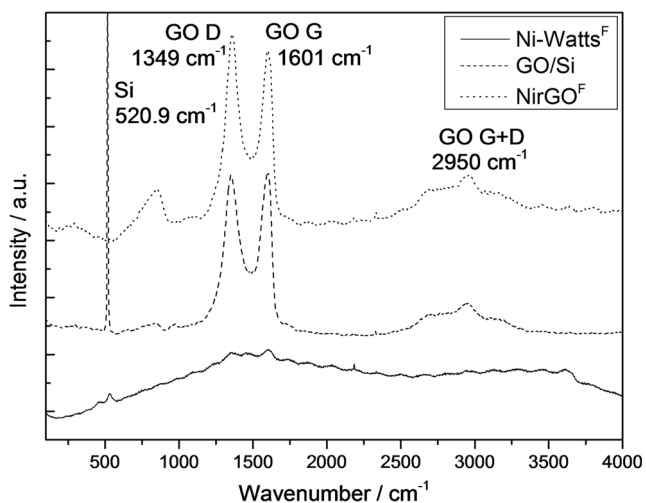
Fig. 2 Raman spectra of fresh synthesized bare Ni-watts electrode, the NirGO sample and a GO blank sample supported on a silicon wafer

corresponds to the first-order scattering of the E_{2g} phonon of sp2 C atoms [35]. The increase in the D peak intensity is an evidence of increase of sp2 domains. The relative intensity ratio of both peaks (I_D/I_G) is a measure of disorder degree and is inversely proportional to the average size of the sp2 clusters [33, 36]. In literature, it is shown that D/G intensity ratio for rGO is larger than that for GO because the domains formed increase the sp2 cluster number [26]. In our case, we have found $I_D > I_G$, by considering the integrated Raman peaks, indicating the presence of rGO in the NirGO catalyst.

The X-ray diffraction patterns (Fig. 3) for Ni-watts and NirGO clearly show the typical reflections expected for nickel with face-centered cubic (fcc) structure without peaks corresponding to impurities.

Values of 2θ for the Ni-watt electrode corresponding to the (1 1 1) and (2 0 0) planes are 44.5° (FWHM = 0.153°) and 51.8° (FWHM = 0.258°), respectively; with a d-spacing distance of 2.03 Å for the (1 1 1) plane and 1.76 Å for the (2 0 0)

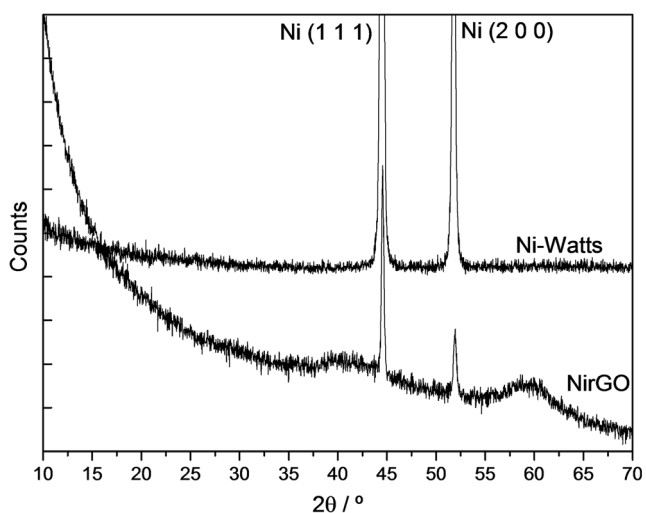**Fig. 3** X-ray diffraction pattern of Ni-watts and NirGO catalysts

plane. Additionally, the values of 2θ for the NirGO electrode corresponding to the (1 1 1) and (2 0 0) planes are 44.6° and 52.0°, respectively, with a d-spacing distance of 2.03 Å for the (1 1 1) plane and 1.76 Å for the (2 0 0) plane, indicating that there is no significant differences between the structures of the nickel in both catalysts.

Short-Term Aging Treatment

The freshly synthesized Ni-watts and NirGO electrodes (denoted as Ni-watts[F] and NirGO[F], respectively), after being characterized with different electrochemical techniques (LSV by RDE and cyclic voltammetry at different temperatures and EIS at different potentials), were subjected to a short-term aging process employing a chronoamperometric pulse at − 1.256 V (vs. RHE) during 4 h in 1 M KOH solution. It can be observed in the chronoamperometric profiles (Fig. S1) that the NirGO electrode has a ~ 15% higher current density than the Ni-watts, and a gradual decrease of the hydrogen generation current is observed in both catalysts related with the deactivation.

The electrode deactivation rate (δ) was calculated as follows [11, 37]:

$$\delta = -\frac{100}{j_e}\left(\frac{dj}{dt}\right) \tag{4}$$

where j_e is the current extrapolated at the start of polarization, and the slope, dj/dt, is evaluated from the linear decay at $t > 2000$ s. The decay rate obtained for Ni-watts and NirGO was 4.9×10^{-3} and 2.2×10^{-3} s^{-1}, respectively. This implies that the NirGO has not only higher electrocatalytic activity than Ni-watts but also deactivates slower due to the aging process.

The aged Ni-watts and NirGO catalysts (denoted as Ni-watts[A] and NirGO[A], respectively) were characterized by the same electrochemical techniques used for the characterization of freshly synthesized samples, and the results are discussed below.

Potentiodynamic Analysis

Figure 4 shows the comparison of cyclic voltammograms without electrode rotation for Ni-watts and NirGO (before and after aging) in alkaline solutions. It can be seen that the Ni-watts catalyst maintains its OP (− 0.71 V vs. RHE) and current density (at − 1.256 V vs. RHE) after aging. On the other hand, the NirGO catalyst after aging maintains the OP (− 0.55 V vs. RHE) of HER (150 mV lower than that observed in electrodeposited Ni-watts), but there is a diminution of the current density. That diminution in the j is originated by the decrease of the (dj/dV) slope of the hydrogen evolution curve by 35%. This loss of activity observed in the NirGO is

Fig. 4 Cyclic voltammograms of Ni-watts and NirGO catalysts in 1 M KOH at 298 K without electrode rotation (scan rate: 10 mV s^{-1})
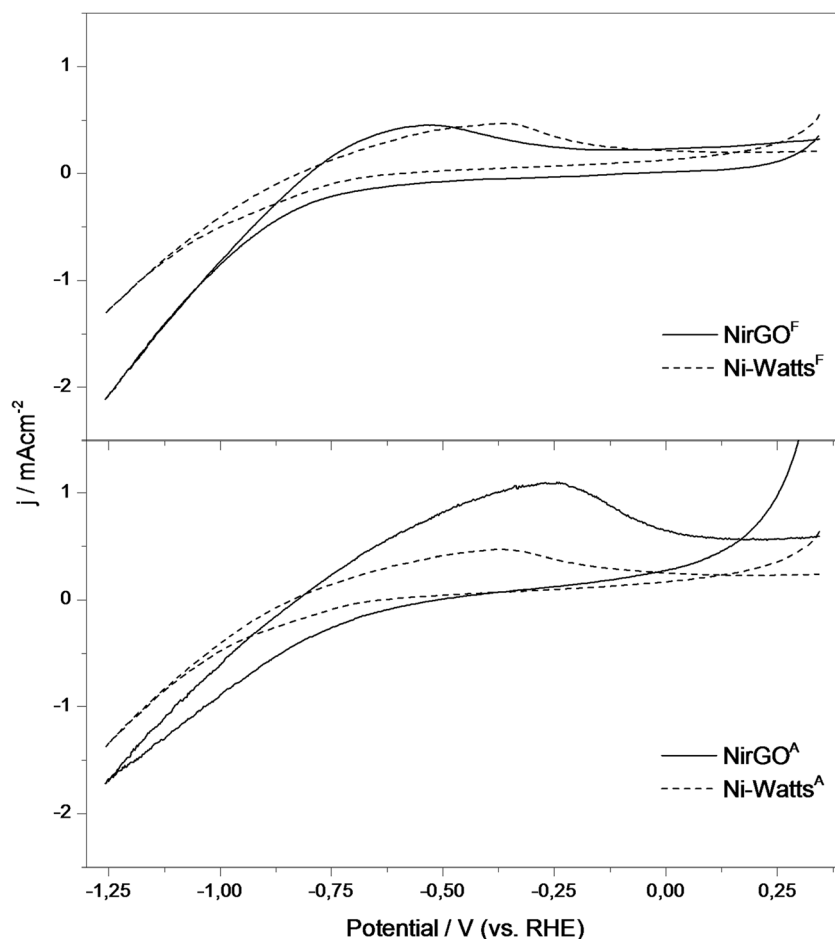
probably due to a stabilization of the surface, due to the presence of rGO. Thus, although the NirGO catalyst suffers a deactivation after the aging process, that loss of activity is compensated by the low OP making the NirGO more electrochemically active than Ni-Watts.

In Fig. 5, the Raman spectra of Ni-watts and NirGO (before and after aging) are shown. It can be seen that NirGO samples maintain the Raman spectrum after aging, whereas samples of Ni-watts after aging show the appearance of bands corresponding to nickel hydrides, related to catalyst aging process. The presence of nickel hydrides is usually associated with the process of loss of activity. Raman is a technique particularly sensitive to the presence of nickel hydrides (particularly when a 488-nm laser for excitation is employed). For this reason, when we observe the presence of nickel hydrides in Ni-watts, we know that a process is occurring that will lead in the subsequent deactivation of the electrode, although this is not currently reflected in the current density. The absence of Raman bands in the NirGO sample (except those corresponding to rGO) indicates that the decrease in current density is due to a rearrangement of the surface and not to a deactivation process by the formation of nickel hydrides.

Figure 6a shows LSV curves for each catalyst before and after the short-term aging measured at 298 K and 1600 rpm. Both catalysts show an increase in the cathodic current after the aging, while the OP remains practically constant. In the case of Ni-watts^A catalyst, an increase of 33% in the current
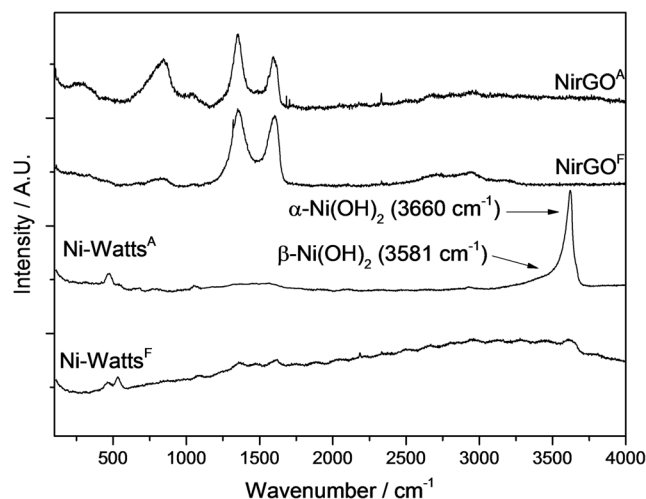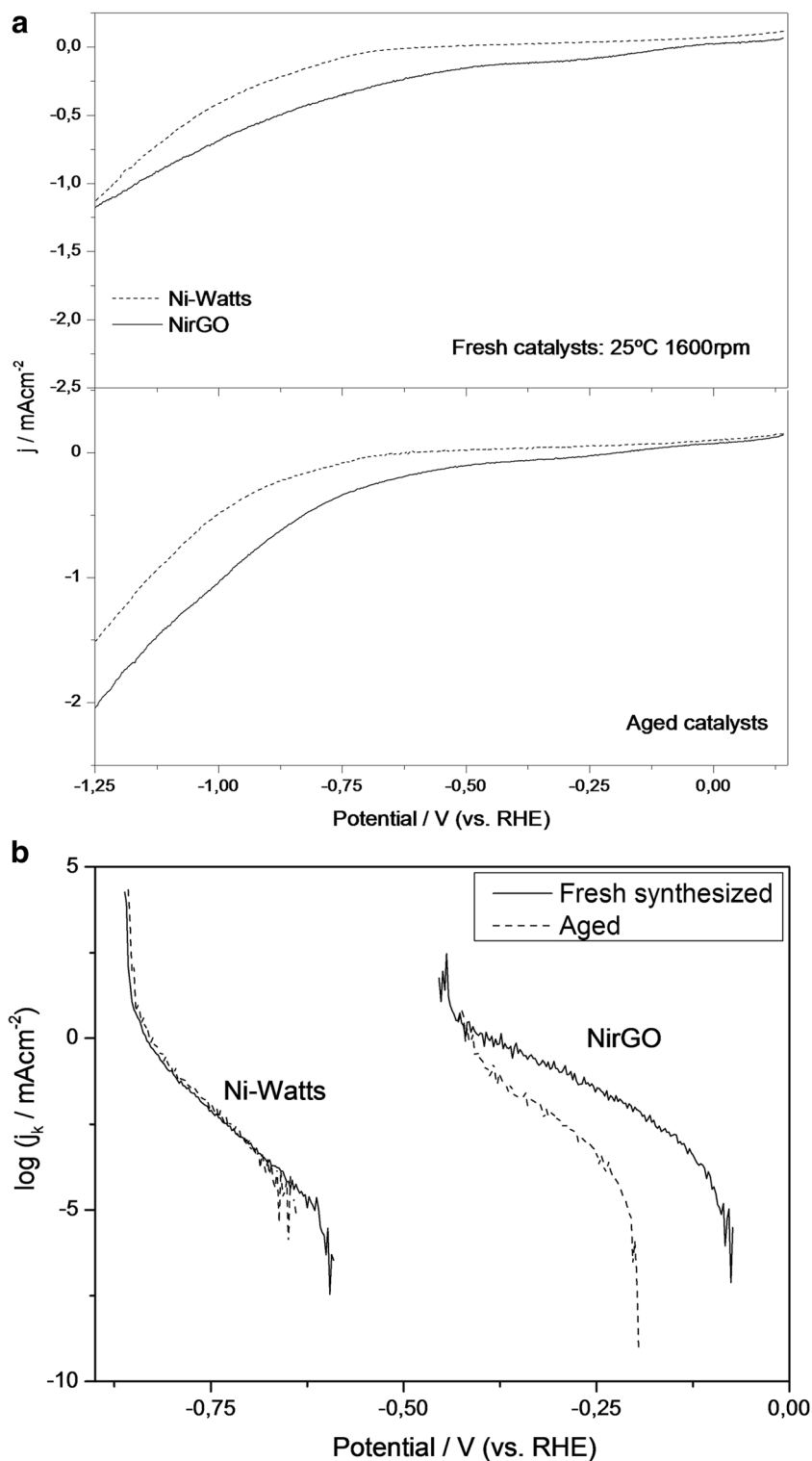

Fig. 5 Raman spectra of bare Ni-watts electrode and the NirGO sample before and after the short aging process (4 h)

Fig. 6 **a** LSV of fresh and aging catalysts in 1 M KOH measured at 298 K (scan rate: 10 mV s^{-1}). **b** Mass transfer corrected Tafel plots for the HER on fresh and aged catalysts measured at 1600 rpm and 293 K. Scan rate = 10 mV s^{-1}

density (at − 1.256 V vs. RHE) is observed. Meanwhile, the NirGO^A catalyst shows an increase much higher (around 75%) in the electrochemical response.

On the other side, values of (dj/dV) slopes are different depending if the characterizations are carried out by CV (without electrode rotation) or LSV (measured at 1600 rpm),

as shown in Fig. 6a and parameters in Table 1. The observed differences are probably due to the fact that both catalysts show different dependence with respect to the diffusional control, which is reflected in the RDE analysis discussed below.

Figure 6b shows the diffusion corrected Tafel curves measured for each catalyst (fresh and aged) at 1600 rpm and

Table 1 Electrochemical and kinetic parameters for the HER on the synthesized catalysts in 1 M KOH, onset potential (OP), Tafel slope (*b*), exchange current density (j_0), and *dj/dV* slopes

	Ni-watts[F]	Ni-watts[A]	NirGO[F]	NirGO[A]
OP/V (vs. RHE)	− 0.71	− 0.71	− 0.55	− 0.55
b/Vdec^{-1}	− 0.056	− 0.056	− 0.083	− 0.079
j_0/mA cm^{-2}	8.0×10^{-5}	8.2×10^{-5}	2.2×10^{-4}	1.8×10^{-4}
CV (*dj/dV*) mAcm^{-2} V^{-1}	3.8	3.7	5.0	3.2
LSV (*dj/dV*) mAcm^{-2} V^{-1}	3.1	2.0	4.3	4.2

298 K. From the Tafel analysis for each catalyst, fresh and aged, Tafel slope values were obtained and are summarized in Table 1. Calculated Tafel slope values are between 0.06 and 0.08 V dec^{-1} for electrodeposited Ni-watts and NirGO catalysts, respectively. All values are lower to that reported in literature for commercial bare Ni (0.13 V dec^{-1}) [38, 39] and are consistent with a reaction where the rate determining step corresponds to a two-electron reaction, indicating a strong contribution of the Heyrovsky step in the global reaction (with a theoretical Tafel slope of 0.0591 V dec^{-1}).

It can be seen in Table 1 that the fresh and aged catalysts exhibit almost the same Tafel slope value. Furthermore, in Fig. 6b, there is no observed changes in Tafel slope, evidence that there are not different reactions to HER, indicating that there is no electrochemical degradation of GO. Furthermore, a large diminution in the equilibrium overpotential is observed. The observed differences in equilibrium potentials are strongly related to the differences in the onset potential of the hydrogen generation reaction, which is much lower in NirGO than in Ni-watts.

The exchange current (j_0) obtained at 298 K and 1600 rpm for NirGO is two times higher than that presented in the electrodeposited Ni-watts electrode (Table 1). Both catalysts show small changes in the j_0 after aging.

In Fig. 7a, a series of LSV curves (measured at different rotation rates), obtained with Ni-watts[F] and NirGO[F] catalysts in 1 M KOH at 298 K, are presented. Significant differences between the electrochemical behaviors of both electrodes are observed. Ni-watts[F] catalyst does not show dependence between the current density and the rotation rate, indicating that the kinetic control is due to charge transfer and not to diffusional control. In the case of the NirGO[F] catalyst, it shows a well-defined charge transfer kinetic control at potentials above − 0.056 V (vs. RHE). A mixed kinetic-diffusion control occurs in the range of − 0.056 to − 0.206 V (vs. RHE) for NirGO[F] catalyst.

Insert in Fig. 7a shows a magnification of the NirGO[F] LSV plot where the change of the current density with the rotation rate evidences the presence of diffusional control. No significant changes are appreciated after aging.

In Fig. 7b, the Koutecky–Levich graphic measured at 298 K for the NirGO[F] catalyst at different potentials is shown and compared to the theoretical curve for the one-electron transference (dashed line). The linearity of the plot indicates that HER is a first-order reaction and a change in j_k (obtained from the $\omega^{-1/2} = 0$ interception) is observed in all the cases [40]. It can be seen that the NirGO catalyst shows an increase in the electron transfer rate with increasing overpotential showing a slow electron transfer [40]. The measured transferred electron number (*n*) value for NirGO[F] catalyst was 1.64. This value of *n* would be indicative of a contribution of the Heyrovsky reaction in the overall mechanisms, as rate determining step.

Electrochemical Impedance Spectroscopy

Figure 8a shows the EIS in the complex plane recorded at the open circuit potential (*E* = − 0.106 V vs. RHE) for NirGO[F] measured at 298 K and 900 rpm. The fit was obtained using a modified Armstrong and Henderson equivalent circuit (AHEC) [28]. In this case, the AHEC was modified by changing the pseudo-capacitance by a CPE component to obtain a satisfactory fit [41]. Insert in Fig. 8a shows the modified AHEC, where R_s is the solution resistance, R_1 is the charge transfer resistance for the electrode reaction, C_1 the double-layer capacitance, and R_2 is related to the superficial mass transfer resistance of H_{ad}.

Both Ni-watts and NirGO catalysts show a similar behavior which is consistent with a charge transfer controlled process.

The impedance spectra in the complex plane were also determined at three electrode potential values, selected to cover the entire HER region: the onset potential of the HER (for each catalyst) and overpotentials of 0.1 and 0.3 V more cathodic than the OP. The two catalysts had similar behaviors to the three selected overpotentials although there is a noticeable change in the charge transfer resistance and capacitance after the aging process. In the case of electrodeposited Ni-watts, variations in the capacitance may be associated with a change in the type of H adsorption, related with the hidruration of the surface [38], while the changes in capacitance and resistance on the NirGO catalyst are much lower than in the case of Ni-watts.

Data in Table 2 indicate that after aging of Ni-watts and NirGO catalysts, there is a diminution of the charge transfer resistances that occurs at the potential of HER (onset potentials and higher overpotentials). Additionally, the NirGO catalyst has lower resistance than the electrodeposited Ni-watts catalyst, which is according to the greater tendency to deactivation of de Ni by formation of hydrides. Furthermore, the diminution in the equilibrium potential and OP is related to that diminution in the charge transfer resistance.

The sum of the resistances $R_1 + R_2$ (for each potential) represents the total faradaic resistance normally related with
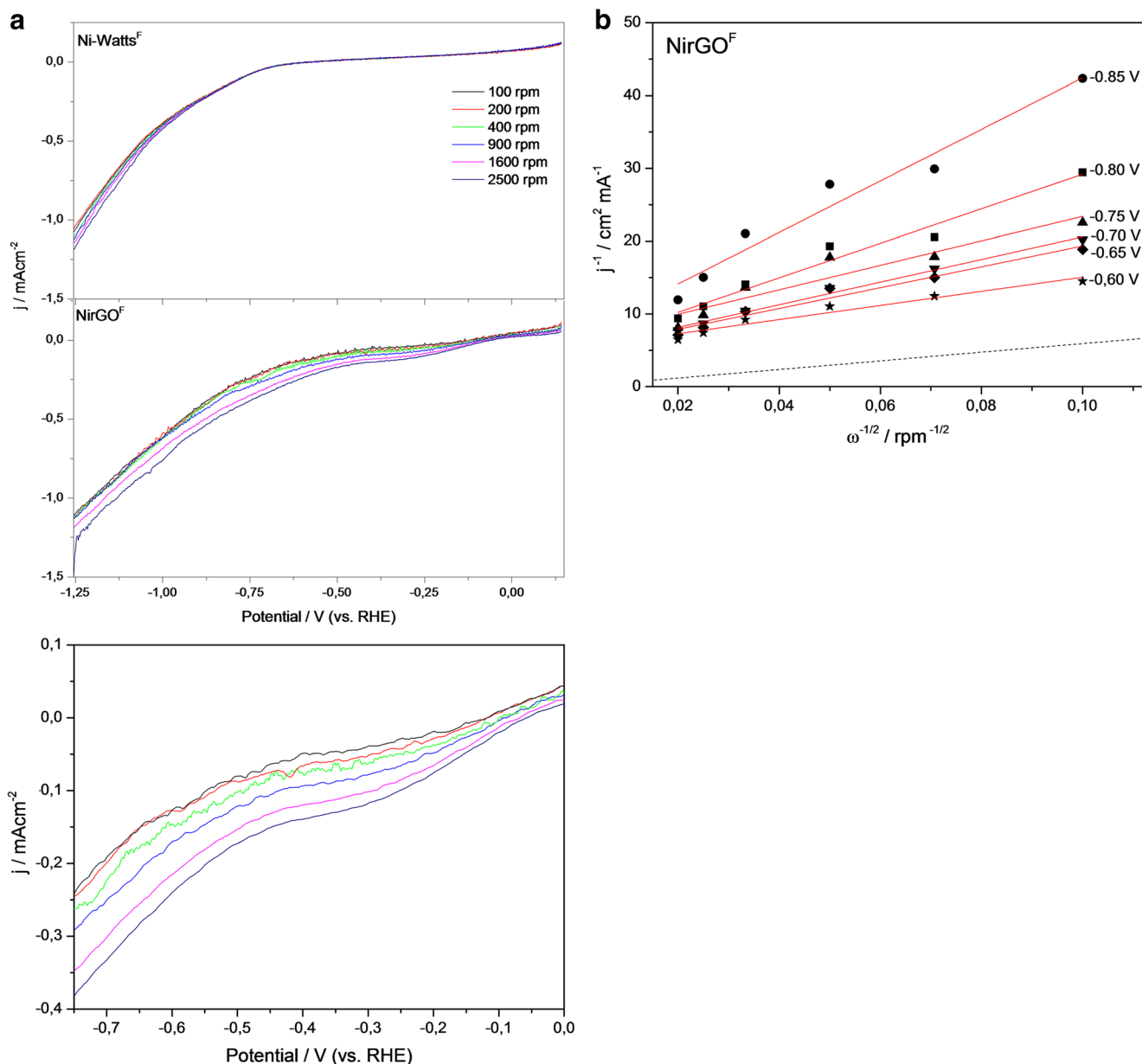
Fig. 7 a Current potential curves for HER obtained in 1 M KOH at 298 K on Ni-watts[F] and NirGO[F] at different rotation rates. Insert: amplification of the diffusion controlled current density on NirGO[F]. **b** K-L plots for HER at 298 K on NirGO at different electrode potentials. The theoretical one electron slope is showed as a dashed line

the HER kinetics. Since the HER is charge transfer controlled (within the considered potential region), the E vs. $log(R_1 + R_2)^{-1}$ plot should be linear, and its slope equal to the Tafel slope, b. Figure 8b, c shows the Tafel plot (without mass transfer correction) along with the simulated E vs. $log(R_1 + R_2)^{-1}$ plot for NirGO[F] and NirGO[A] catalysts. The graphs obtained for fresh and aged Ni-watts catalysts (not shown) are similar to those presented in Fig. 8a. The separation between the Tafel curve ($log j$) and the $log(R_1 + R_2)^{-1}$ observed for the Ni-watts[F] catalyst was 1.35 ± 0.1, close to the theoretical separation for Langmuir type adsorption (1289) [42], and the separation for the Ni-watts[A] catalyst was 1.65 (indicating a

Temkin type adsorption characterized by a theoretical separation of 1.86) [42]. This change in the adsorption type was previously reported and attributed to the formation of hydrides of the catalyst surface [38]. NirGO catalysts (fresh and aged) show a separation of 1.81 and 1.65, respectively, indicating a Temkin type adsorption.

Temkin type hydrogen adsorption is usually associated with the formation of a nickel hydride layer, responsible for the loss of electrocatalytic activity [38, 43], but those nickel hydrides are not observed in the NirGO catalyst (Fig. 5), so that we suppose that the change in the adsorption type is due to the presence of the GO in the matrix of the catalyst.
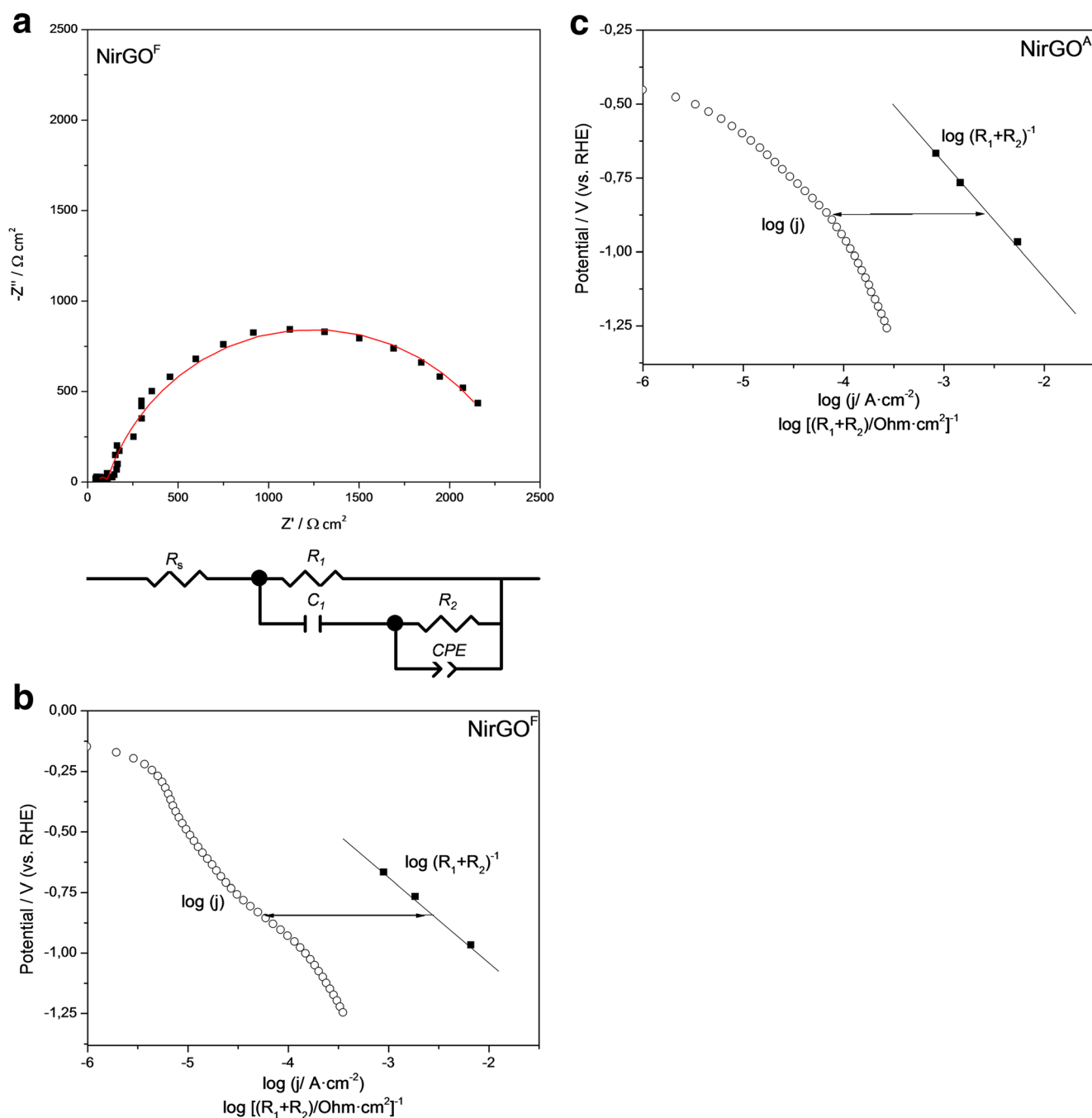
Fig. 8 **a** Nyquist plot impedance spectra in the complex plane for the HER on NirGO^F (filled dots) and NirGO^A (open dots) in 1 M KOH at 298 K and at a rotation rate of 900 rpm at the OCP. The solid lines are calculated using the modified AHEC. Insert in **a** modified Armstrong and Henderson equivalent circuit. **b** Experimental Tafel plot (circled points) and simulated E-log($R_1 + R_2$)$^{-1}$ plot (squares) with the corresponding linear fit (dahsed line) for the HER in 1 M KOH solution at 298 K, on NirGO^F and **c** NirGO^A

Conclusions

In this paper, a simple and reproducible co-deposition method for the synthesis of nickel/reduced graphene oxide hybrid catalysts is presented and the electrocatalysis of hydrogen evolution reaction was studied with both the hybrid catalyst and the pure electroplated nickel. The presented method is easily scalable to industrial level so can be used to economically improve electrodeposited nickel electrodes for HER.

The electrochemical results show that GO is reduced during catalyst synthesis giving high conductivity rGO, significantly decreasing the charge transfer rate and resistance presented by pure nickel electrodeposits.

Table 2 Parameters of the modified AHEC for the HER in 1 M KOH at 298 K at the open circuit potential (OCP) and the onset potential (OP) of the HER

Catalyst	E/V (RHE)	$R_1/\Omega\ cm^2$	$R_2/\Omega\ cm^2$	$C_p/F\ cm^{-2}$	$CPE/F\ cm^{-2}$
Ni-watts[F]	− 0.12 (OCP)	69.2	48,774	1.23×10^{-6}	1.08×10^{-4}
	− 0.71 (OP)	102.2	30,065	2.76×10^{-9}	9.09×10^{-4}
Ni-watts[A]	− 0.12 (OCP)	104.2	32,062	1.33×10^{-6}	1.14×10^{-4}
	− 0.71 (OP)	53.68	3391	7.45×10^{-7}	5.34×10^{-4}
NirGO[F]	− 0.12 (OCP)	28.25	3327	3.63×10^{-6}	6.32×10^{-4}
	− 0.55 (OP)	18.94	1271	3.38×10^{-6}	1.43×10^{-4}
NirGO[A]	− 0.12 (OCP)	59.19	2118	2.49×10^{-4}	4.64×10^{-4}
	− 0.55 (OP)	32.18	1171	1.37×10^{-5}	9.49×10^{-4}

It can be seen that both catalysts behave differently in terms of variations of the *(dj/dV)* slopes when characterized via cyclic voltammetry (measured without electrode rotation) and linear sweep voltammetry (measured at 1600 rpm). The differences observed in the *(dj/dV)* slopes during the CV and LSV are due to the fact that catalysts show different dependencies on the diffusional control, indicating that the NirGO catalyst possibly has better performance on systems with flow electrolyzers.

Moreover, NirGO catalyst surface shows no presence of hydrides, unlike electrodeposited Ni-watts catalyst in the Raman spectra. Changes in the hydrogen adsorption type can be seen in studies EIS and correlate with the results obtained by Raman showing a clear inhibition in the formation of surface hydrides due to the presence of reduced graphene oxide in the catalyst structure.

References

1. J.O.M. Bockris, T.N. Veziroglu, Int. J. Hydrog. Energy **32**, 1605 (2007)
2. M.D. Symes, L. Cronin, Nat. Chem. **5**, 403 (2013)
3. M. Ball, M. Weeda, (2016) The hydrogen economy—Vision or reality?, Compendium of Hydrogen Energy, Volume 4: Hydrogen Use, Safety and the Hydrogen Economy, 237
4. A. Bakenne, W. Nuttall, N. Kazantzis, Int. J. Hydrog. Energy **41**, 7744 (2016)
5. D. Pletcher, L. Xiaohong, Int. J. Hydrog. Energy **36**, 15089 (2011)
6. K. Zeng, D. Zhang, Prog. Energy Combust. Sci. **36**, 307 (2010)
7. F.A. Viva, M.M. Bruno, E.A. Franceschini, Y.R.J. Thomas, G. Ramos Sanchez, O. Solorza-Feria, H.R. Corti, Int. J. Hydrog. Energy **39**, 8821 (2014)
8. Z. Hong, X. Li, S.-Z. Kang, L. Qin, G. Li, J. Mu, Int. J. Hydrog. Energy **40**, 14297 (2015)
9. M.A. McArthur, L. Jorge, S. Coulombe, S. Omanovic, J. Power Sources **266**, 365 (2014)
10. M.H. Tang, C. Hahn, A.J. Klobuchar, J.W. Desmond, J. Wellendorff, T. Bligaard, T.F. Jaramillo, Phys. Chem. Chem. Phys. **16**, 19250 (2014)
11. E.A. Franceschini, M.M. Bruno, F.J. Williams, F.A. Viva, H.R. Corti, ACS Appl. Mater. Interfaces **5**, 10437 (2013)
12. S. Ruiz-Gómez, A. Boscá, L. Pérez, J. Pedrós, J. Martínez, A. Páez, F. Calle, Diamond. Relat. Mater **57**, 63 (2015)
13. J. Wang, T. Qiu, X. Chen, Y. Lu, W. Yang, J. Power Sources **293**, 178 (2015)
14. Y. Zheng, Y. Jiao, L.H. Li, T. Xing, Y. Chen, M. Jaroniec, S.Z. Qiao, ACS Nano **8**, 5290 (2014)
15. G. Xie, K. Zhang, B. Guo, Q. Liu, L. Fang, J.R. Gong, Adv. Mater. **25**, 3820 (2013)
16. J. Zhu, Y. Kumar Sharma, Z. Zeng, X. Zhang, M. Srinivasan, S. Mhaisalkar, H. Zhang, H. Hoon Hng, Q. Yan, J. Phys. Chem. C **115**, 8400 (2011)
17. Y. Tao, L. Ruiyi, Z. Haiyan, L. Zaijun, Mater. Res. Bull. **78**, 163 (2016)
18. W.-L. Song, X. Li, L.-Z. Fan, Energy Storage Mater **3**, 113 (2016)
19. J. Balamurugan, G. Karthikeyan, T.D. Thanh, N.H. Kim, J.H. Lee, J. Power Sources **308**, 149 (2016)
20. D. Akyüz, B. Keskin, U. Şahintürk, A. Koca, Appl. Catal. B Environ. **188**, 217 (2016)
21. Y.-G. Huang, H.-L. Fan, Z.-K. Chen, C.-B. Gu, M.-X. Sun, H.-Q. Wang, Q.-Y. Li, Int. J. Hydrog. Energy **41**, 3786 (2016)
22. M. Zhiani, S. Kamali, Electrocatalysis **7**(6), 466 (2016)
23. A.K. Geim, K.S. Novoselov, Nat. Mater. **6**, 183 (2007)
24. S. Seetharaman, R. Balaji, K. Ramya, K.S. Dhathathreyan, M. Velan, Int. J. Hydrog. Energy **38**, 14934 (2013)
25. S. Yang, B. Deng, R. Ge, L. Zhang, H. Wang, Z. Zhang, W. Zhu, G. Wang, Nanoscale Res. Lett. **9**, 672 (2014)
26. G. Sobon, J. Sotor, J. Jagiello, R. Kozinski, M. Zdrojek, M. Holdynski, P. Paletko, J. Boguslawski, L. Lipinska, K.M. Abramskim, Opt. Express **13**, 19463 (2012)
27. J. Rodríguez-Carvajal, Physica B **195**, 55 (1993)
28. R.D. Armstrong, M. Henderson, J. Electroanal. Chem. **39**, 81 (1972)
29. E.A. Franceschini, G.I. Lacconi, H.R. Corti, J. Energ. Chem. **26**, 466 (2017)
30. E.A. Franceschini, G.I. Lacconi, H.R. Corti, Int. J. Hydrogen Energ. **41**, 3326 (2016)
31. E.A. Franceschini, M.M. Bruno, F.A. Viva, F.J. Williams, M. Jobbágy, H.R. Corti, Electrochim. Acta **71**, 173 (2012)
32. D.S. Hall, C. Bock, B.R. MacDougall, J. Electrochem. Soc. **160**, F235 (2013)
33. Y. Guo, X. Sun, Y. Liu, W. Wang, H. Qiu, J. Gao, Carbon **50**, 2513 (2012)

34. A. Jorio, M. Dresselhaus, R. Saito, G.F. Dresselhaus, *Raman Spectroscopy in Graphene Related Systems* (Wiley-VCH, Germany, 2011)
35. A.C. Ferrari, J. Robertson, Phys. Rev. B **61**, 14095 (2000)
36. O. Akhavana, E. Ghaderia, Carbon **50**, 1853 (2012)
37. M.M. Bruno, E.A. Franceschini, G.A. Planes, H.R. Corti, J. Appl. Electrochem. **40**, 257 (2010)
38. E.A. Franceschini, G.I. Lacconi, H.R. Corti, Electrochim. Acta **159**, 210 (2015)
39. G. Kreysa, B. Hakansson, P. Ekdunge, Electrochim. Acta **33**, 1351 (1988)
40. R.W. Zurilla, R.K. Sen, E. Yeager, J. Electrochem. Soc. Electrochem. Sci. Tech. **125**, 1103 (1978)
41. A. Damian, S. Omanovic, J. Power Sources **158**, 464 (2006)
42. L. Bai, D.A. Harrington, B.E. Conway, Electrochim. Acta **32**, 1713 (1987)
43. D.S. Hall, D.J. Lockwood, S. Poirier, C. Bock, B.R. MacDougall, ACS Appl. Mater. Interfaces **6**, 3141 (2014)